RSC Advances

PAPER

View Article Online
View Journal | View Issue

Cite this: *RSC Adv.*, 2025, **15**, 21528

Tagetes erecta synthesized bimetallic Ag–Au nanoparticles and their potential application in electrochemical detection and estimation of ampicillin in raw milk†

Surbhi Kumari, Rishika Rohilla, Sonia Rani and Nirmal Prabhakar *

This study focuses on the green synthesis of Ag–Au nanoparticles using *Tagetes erecta* extract and their potential application in electrochemical detection and estimation of ampicillin in raw milk. The synthesised nanoparticles were characterized using both physical as well as electrochemical techniques to assess their structural, morphological and conductive properties. The Ag–Au nanoparticles were covalently bonded to the hydroxylated fluorine doped tin oxide electrode surface through silane chemistry enabling the effective interaction of the 5′ thiolated-aptamer with the nanoparticle-modified surface for aptasensor development. The proposed aptasensor displayed a highly sensitive and selective electrochemical response towards ampicillin within a range of 0.1 ng mL^{-1} to 1000 ng mL^{-1} with a limit of detection of 0.40 ng mL^{-1} and a shelf-life of 30 days. Moreover, the aptasensor demonstrated reliable performance with both spiked milk samples and real milk samples, detecting a concentration of 194 ng mL^{-1} in raw milk with results closely matching with those obtained by LC-MS. Therefore, this study highlights the feasibility of plant-based nanoparticle synthesis for developing cost-effective and efficient electrochemical sensors in food safety monitoring.

Received 30th April 2025
Accepted 17th June 2025

DOI: 10.1039/d5ra03037d

rsc.li/rsc-advances

1 Introduction

Ensuring food safety is a global priority, particularly in dairy products like milk. Since ancient times, milk has been an integral part of the human diet, serving as the first source of nutrition and often regarded as nature's complete food.[1] The safety and quality of milk can be compromised by various contaminants, including antibiotic residues (ARs). These residues primarily originate from the administration of antibiotics to dairy animals for disease prevention. If proper withdrawal periods are not observed before milking, antibiotics can persist in milk.[2] Additionally, AR(s) can also be found due to improper disposal of medicated feed or water, as well as the use of antibiotics for the treatment of infections such as mastitis or as growth promoters.[3] Among various antibiotic classes, beta-lactam antibiotics are the most widely used in dairy farming due to their broad-spectrum activity and effectiveness against bacterial infections.[4,5]

Amongst beta-lactams, ampicillin (AMP) is extensively used antibiotic in veterinary medicine, particularly for treating bacterial infections in animals. And since milk is a staple in many households worldwide, valued for its nutritional benefits and taste, presence of these antibiotics in milk can pose serious health risks including allergic reactions, development of antimicrobial resistance, and non-allergic hypersensitivity reactions including gastrointestinal disturbances and skin rashes to consumers.[6,7] Acknowledging the risks associated with ARs, regulatory agencies have established guidelines to safeguard milk safety. As per the Food Safety and Standards Authority of India (FSSAI) the strict maximum residue limits (MRLs) for ampicillin is 0.01 mg kg^{-1} of body.[8] The detection of ampicillin in milk samples is usually performed using traditional analytical techniques such as ELISA,[9] LC-MS,[10] and other immunological methods.[11] While these techniques offer high sensitivity, their practical application is hindered by complex instrumentation, the need for skilled personnel, and high operational costs. These limitations make them less suitable for routine analysis. This necessitates the development of sensitive and selective detection methods with simple operation and high accuracy to monitor public health safety.

Biosensors have emerged as powerful tools for detecting trace-level targets, offering high sensitivity, rapid response, and portability for effective monitoring. It is widely acknowledged that, among different types of biosensors, electrochemical biosensors present a promising alternative due to their high sensitivity and precision in analytical applications.[12,13] Notably, electrochemical techniques provide a broad dynamic range and

Department of Biochemistry, Panjab University, Chandigarh 160014, India. E-mail: nirmalprabhakar@gmail.com

† Electronic supplementary information (ESI) available. See DOI: https://doi.org/10.1039/d5ra03037d

require minimal sample volumes.[14] Coupled with their exceptionally low detection limits, they enable the analysis of analytes at low levels. Certainly, electrochemical methods require modifying the electrode surface to improve the reactions, making the process more efficient.

Nanomaterial-based surface modifications play a crucial role in this enhancement and adopting a green synthesis approach for nanoparticles synthesis is a sustainable and eco-friendly strategy due to its cost-effectiveness and biocompatibility, along with valuable properties such as antibacterial activity, optical characteristics, and conductivity.[15] Also, the use of natural resources such as plant extracts, biomass, waste, non-toxic bacteria, algae for nanoparticle synthesis eliminates the need for toxic reducing and stabilizing agents, unlike conventional techniques which often involve the use of toxic chemicals and high energy consumption for the synthesis and stabilization of nanoparticles.[16,17] The effectiveness of green synthesis lies in its utilization of bioactive compounds, such as polyphenols, flavonoids, and proteins, which contain functional parts that act as reducing and stabilizing agents for the nanoparticle precursors facilitating the reduction of metal ions, growth and stabilization of nanoparticles, ensuring controlled morphology and stability.[18,19] Ghasemi *et al.* 2025 utilized *Ferula gummosa* Boiss. gum extract for the synthesis of silver nanoparticles, exploring their potential application in breast cancer therapy.[20] El-Said *et al.* synthesized carbon dots/gold nanoparticles composite from pomegranate juice using green approach for the sensing of neurotransmitters.[21] Plant extracts from fruit peels, leaves, seeds, and vegetable residues are being effectively used for the green synthesis of various nanoparticles and are being utilized in a wide range of applications.[22–24]

While, Padalia *et al.* synthesized silver nanoparticles using marigold flower extract.[25] This study is the first to explore electrochemical detection and estimation of beta-lactam class belonging antibiotic "ampicillin" in raw milk using bimetallic silver–gold nanoparticles (Ag–Au NPs) synthesized from *Tagetes erecta* extract. Bimetallic Ag–Au NPs offer exceptional advantages for electrochemical sensing due to their enhanced conductivity, high surface area to volume ratio, and excellent catalytic properties. In addition to this, the synergistic interaction between silver and gold improves electron transfer kinetics, leading to increased sensitivity and lower detection limits in electrochemical measurements. Their large surface area provides more active sites for the immobilization of biomolecules, facilitating strong analyte interactions and improving overall performance of the sensor. As well as, if engineered correctly, green synthesized Ag–Au NPs exhibit excellent stability and biocompatibility. Their ability to amplify electrochemical signals enables the detection of trace amounts of analytes, making them suitable for biosensing applications. Therefore, the integration of green synthesized bimetallic Ag–Au NPs provides enhanced sensitivity, selectivity, and stability to the proposed aptasensor, enabling real-time monitoring of ampicillin in raw milk, critical for ensuring food safety and quality.

2 Experimental section

2.1 Chemicals

All chemicals were of analytical grade, and the solutions were prepared with autoclaved de-ionized water (dH_2O). Acetonitrile, acetic acid, sodium dihydrogen orthophosphate ($NaH_2PO_4 \cdot 2H_2O$), disodium hydrogen orthophosphate anhydrous (Na_2HPO_4), sodium hydroxide (NaOH), hydrochloric acid (HCL), potassium ferricyanide [$K_3Fe(CN)_6$], potassium ferrocyanide trihydrate [$K_4Fe(CN)_6 \cdot 3H_2O$], tris hydroxymethyl aminomethane (Tris HCL), ethylenediamine tetra acetic acid (EDTA) were procured from HI Media Laboratories Pvt. Ltd. Ammonium hydroxide (NH_4OH), hydrogen peroxide (H_2O_2), methanol, chloroauric acid ($HAuCl_4 \cdot 3H_2O$), silver nitrate ($AgNO_3$), (3-mercaptopropyl)trimethoxysilane (MPTS), 6-mercapto-1-hexanol (MCH) were procured from Sigma-Aldrich. Ampicillin salt was obtained from Zene X. The Thiolated-aptamer was purchased from Sigma-Aldrich and is taken from published literature.[26] The sequence of the aptamer is as follows.

5′-[SH] TTA GTT GGG GTT CAG TTG G-3′

2.2 Instrumentations

Electrochemical studies, including Differential Pulse Voltammetry (DPV), Cyclic Voltammetry (CV), and Electrochemical Impedance Spectroscopy (EIS), were conducted using an AutoLab potentiostat/galvanostat [AutoLab302NFRA32M]. All the experiments were performed using a three-electrode system, where fluorine-doped tin oxide (FTO) electrode served as working electrode, Ag/AgCl as reference electrode and a platinum wire as counter electrode. The physical characterization studies of the working electrode were carried out using field emission scanning electron microscopy (Hitachi SU8010), high resolution transmission electron microscopy (JEOL JEM 2100 plus), Fourier transform infrared spectroscopy (PerkinElmer, spectrum II), UV spectrophotometer (Shimadzu), dynamic light scattering and ZETA potential (Litesizer 500 Anton Paar).

2.3 Green synthesis of Ag–Au NPs

The synthesis of bimetallic Ag–Au NPs was successfully carried out using an environment-friendly method utilizing marigold flower (*Tagetes erecta*) petals extract as the reducing and stabilizing agent.

2.3.1 Preparation of flower extract. Marigold flower petals were taken and thoroughly rinsed twice with distilled water before being air-dried. A total of 10 g of dried and pulverized petals were then immersed in 50 mL of boiling water for 12 min. The resulting mixture was then filtered and the supernatant containing the bioactive compounds was collected for further use and stored in the refrigerator.

2.3.2 Synthesis of Ag NPs. For the synthesis of silver NPs, 40 mL of distilled water was taken in a beaker, and 2 mM $AgNO_3$ was added as a precursor. The solution was then heated to 50 °C with continuous stirring for 15 minutes, followed by dropwise addition of marigold extract. A noticeable change of colour from colourless to dark yellowish-brown was observed, indicating the formation of Ag NPs. The solution was further incubated for 24

hours with continuous stirring to form stable particles. The resulting solution was then centrifuged for 4 cycles at 8481×*g* RCF for 15 min at 25 °C followed by washing with distilled water and ethanol to remove any impurity. The pellets obtained after centrifugation were dissolved in 1 mL distilled water.[25]

2.3.3 Synthesis of Au NPs. Gold NPs were synthesized by dissolving 1 mM $HAuCl_4$ in 40 mL of distilled water, heating the solution to 50 °C, and subsequently adding the plant extract dropwise into the precursor solution. A colour transition from light yellow to dark reddish-black, indicates Au NPs formation. The reaction mixture was continuously stirred and incubated for 5 hours to ensure complete synthesis. The synthesized NPs were purified *via* centrifugation at 8481×*g* RCF for 15 minutes at 25 °C, followed by multiple washing steps to eliminate residual impurities. The obtained pellet was resuspended in 1 mL of distilled water for further use.

2.3.4 Post-synthesis assembly. The formed NPs were dissolved in 30 mL distilled water and ultrasonicated in a probe sonicator for 3 hours with addition of 2 mL extract. The particles were again centrifuged at 4226×*g* RCF for 20 min followed by washing with distilled water and ethanol to remove any impurity. The obtained solution was then kept in rotary evaporator to obtain Ag–Au powdered NPs.

Obtained NPs were then characterized by UV-vis spectrophotometry (UV), field emission scanning electron microscopy (FE-SEM), high resolution – transmission electron microscopy (HR-TEM), dynamic light scattering (DLS), zeta potential (ZETA), and electrochemical techniques such as cyclic voltammetry (CV), differential pulse voltammetry (DPV) and, electrochemical impedance spectroscopy (EIS).

2.4 Preparation of immobilization platform

An initial hydroxylation treatment was given to FTO electrodes by dipping in a solution containing NH_4OH, H_2O_2 and H_2O in a 1 : 1 : 5 ratio and incubating them in an oven at 60 °C for 40 min. This step introduces hydroxyl groups onto the FTO surface which facilitate the reaction with (3-mercaptopropyl) trimethoxysilane (MPTS), ensuring its strong adherence to the electrode. Subsequently, the hydroxylated FTOs were dipped in 1.0×10^{-3} mol L^{-1} solution of MPTS in methanol for 12 hours, allowing silane functionalization through covalent bonding.[27] Further, 10 μL of Ag–Au bimetallic NPs (1 mg mL^{-1}) were drop cast onto the MPTS modified electrode. The green-synthesized Ag–Au NPs bind with the SH group of (3-mercaptopropyl)trimethoxysilane *via* strong thiol-metal affinity, forming a stable Au–S or Ag–S bond.[28,29]

2.5 Fabrication of aptasensor for the detection of ampicillin

The development of the aptasensor is based on the interaction between 5′ thiolated-aptamer and Ag–Au NPs deposited electrode surface as illustrated in Scheme 1. The ampicillin specific thiolated-aptamer stock solution was made in TE buffer prepared by mixing 10 mM Tris HCl (pH 7.5) and 1 mM EDTA (pH 8.0) in 5 : 1 ratio. 5 μL of optimized concentration *i.e.* 10 μM thiolated aptamer was applied to Ag–Au/MPTS/FTO electrodes and incubated for 90 minutes. Furthermore, 10 μL of a 50 mM 6-mercaptohexanol (MCH) solution was applied to the aptamer-functionalized electrode for about 1 h at room temperature to prevent non-specific adsorption. The modified electrodes were then rinsed with 0.1 M PBS to remove any unbound aptamer molecules. Finally, 10 μL of 1 ng per mL ampicillin solution, prepared in sterile water, was drop-casted onto the apta-electrode and incubated for an optimized response time of 15 minutes at room temperature.

2.6 Electrochemical aptasensing of ampicillin

For the electrochemical detection of ampicillin, a 1 mg mL^{-1} stock solution was prepared in sterile water, then serially diluted to make the concentration range varying from 0.1 ng mL^{-1} to 1 mg mL^{-1}. Further, the fabricated apta-electrode was incubated with 10 μL of a known concentration of ampicillin for 15 min at room temperature (Section 3.3). After incubation, the electrodes were allowed to dry and thoroughly washed to remove any weakly attached molecules. Finally, the ampicillin concentration was measured using the DPV technique, and the anodic peak current values were recorded, which were further utilized to calculate analytical parameters such as limit of detection (LOD).

3 Results and discussion

3.1 Physical characterization

The successful formation of Ag and Au NPs was initially confirmed using UV spectroscopy technique. Fig. 1A(i) shows the UV spectrum of Ag NPs, which reveals a characteristic peak at 419 nm, indicating the successful synthesis of Ag NPs. Fig. 1A(ii) displays the UV spectrum of Au NPs, with a characteristic peak at 531.5 nm, confirming the formation of Au NPs. Further, Fig. 1A(iii) reveals a single broad peak at 417 nm for the colloidal Ag–Au NPs, after the post-synthesis modifications, thereby confirming the successful formation of bimetallic Ag–Au NPs[30].

The morphological features of the electrodes after each modification step are examined by FE-SEM technique. Fig. 1B shows SEM images of (i) MPTS/FTO, (ii) Ag–Au/MPTS/FTO, (iii) aptamer/Ag–Au/MPTS/FTO electrodes at magnifications of 1 μm and 400 nm. Fig. 1B(i) shows the FE-SEM image of MPTS/FTO electrode revealing no major change in surface morphology but a transparent thin layer of MPTS. Further, oval shaped particles were seen in FE-SEM image of Ag–Au/MPTS/FTO electrode at a magnification of 400 nm (Fig. 1B(ii)), uniform deposition reveals a strong adherence of the particles to the electrode surface. This can be attributed to the strong affinity of metals for thiol group. Furthermore, Fig. 1B(iii) reveals the binding of the thiolated-aptamer to the Ag–Au NPs modified surface, showing a noticeable change in surface morphology forming a uniform thick layer on the electrode surface. The binding at each step was also verified by EDS analysis (Fig. 1C). The EDS spectra of Ag–Au/MPTS/FTO depicted the presence of C (16.62%), O (74.35%), Si (1.99%), S (0.22%) which verified the silanization of FTO electrode surface. The presence of Ag (6.19%) and Au (0.64%) ascertains the deposition of NPs on the

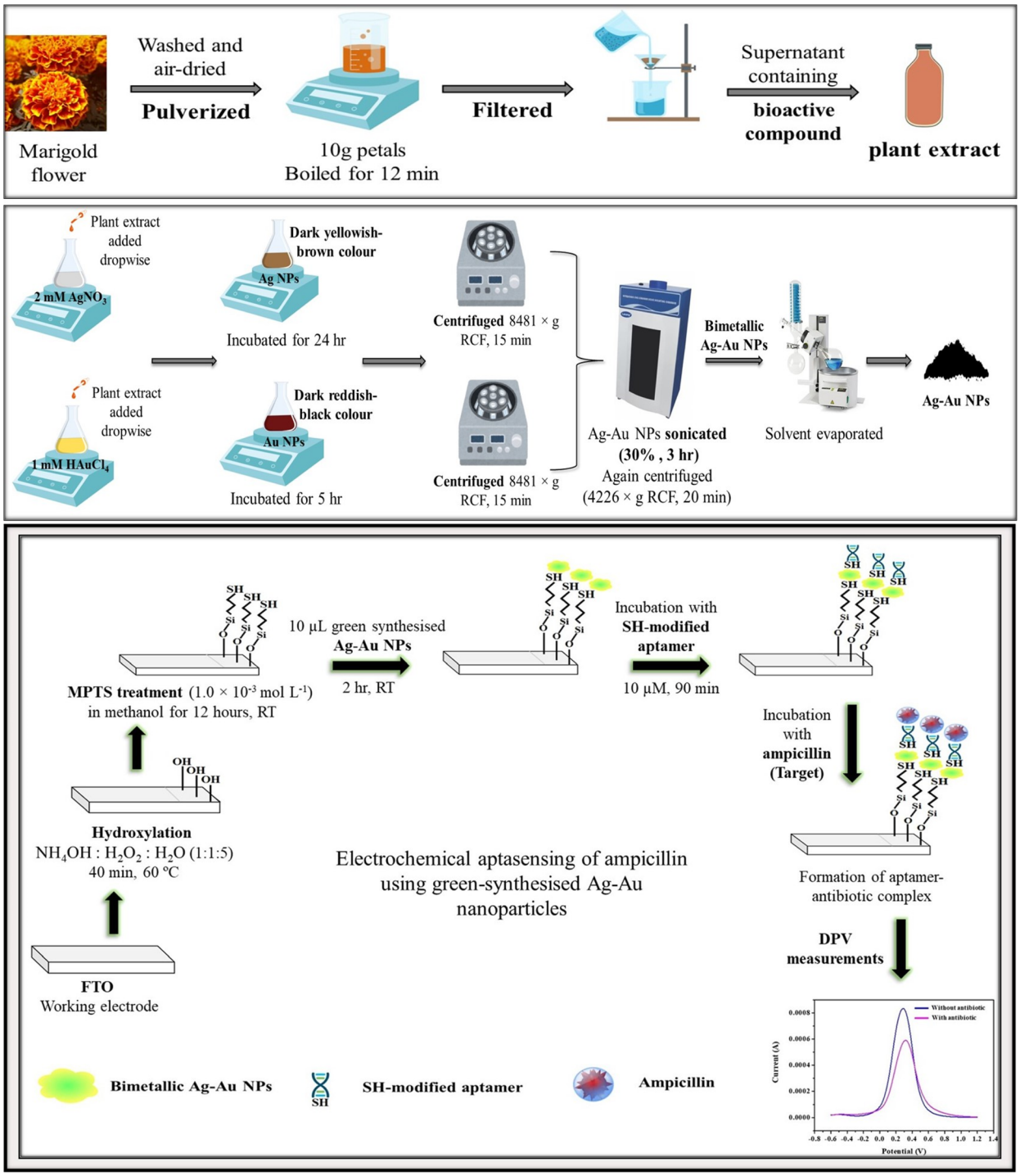

Scheme 1 Schematic representation of green-synthesis of Ag–Au nanoparticles and their application in electrochemical aptasensing of ampicillin.

electrode surface. Also, elemental mapping analysis (Fig. S1†) demonstrated the uniform deposition of each element confirming the fabrication of Ag–Au/MPTS/FTO electrode.

Fig. 2A shows the HRTEM images of Ag NPs, Au NPs, and bimetallic Ag–Au NPs, respectively. TEM provides precise information regarding the shape, morphology, and size of the synthesized NPs. The images confirm that both Ag and Au NPs exhibit spherical morphologies with an average diameter ranging from 15 to 20 nm. While, the bimetallic Ag–Au NPs also display a spherical shape, with a larger average size of approximately 32 nm. The HRTEM images indicate uniform dispersion of the nanoparticles. Compared to the monometallic Ag and Au NPs, the bimetallic Ag–Au NPs display clearly visible lattice

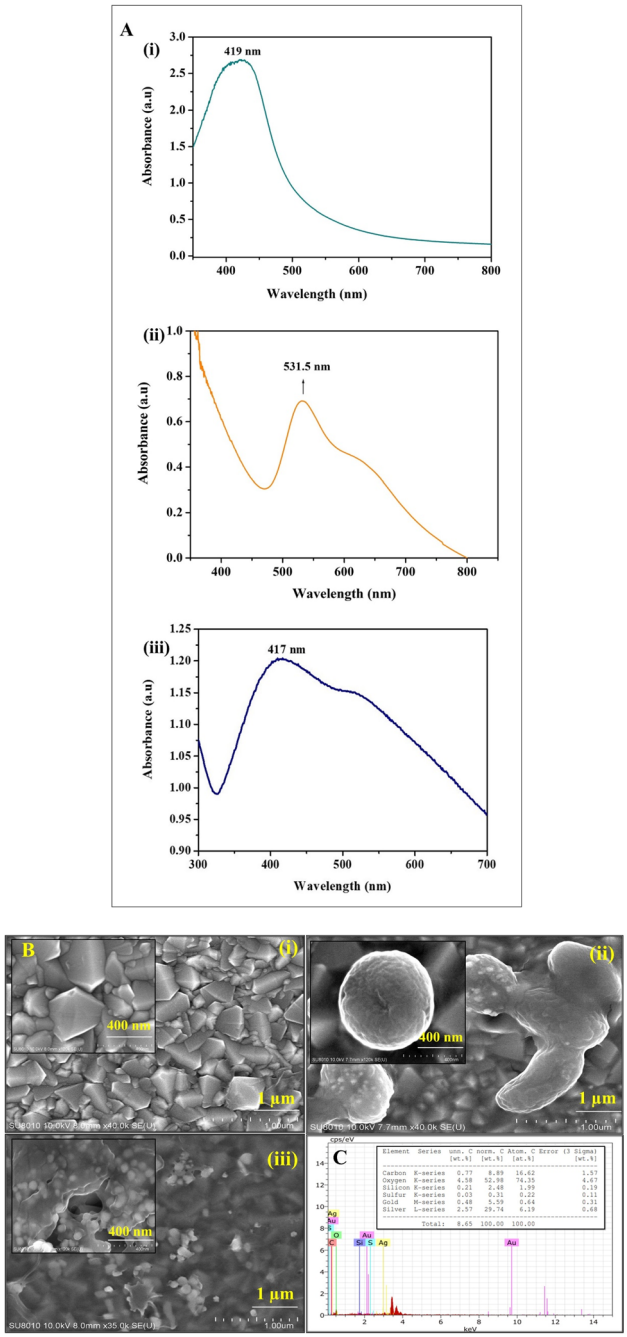

Fig. 1 Physical Characterization (A) UV spectrum of (i) Ag NPs, (ii) Au NPs, (iii) Bimetallic Ag–Au NPs, (B) FE-SEM images of (i) MPTS/FTO electrode at a magnification of 1 µm and inset represents image at a magnification of 400 nm, (ii) Ag–Au/MPTS/FTO at a magnification of 1 µm and inset represents image at a magnification of 400 nm, (iii) aptamer/Ag–Au/MPTS/FTO at a magnification of 1 µm and inset represents image at a magnification of 400 nm, (C) EDS spectra of Ag–Au/MPTS/FTO electrode and the inset represents all the elements present on the modified electrode.

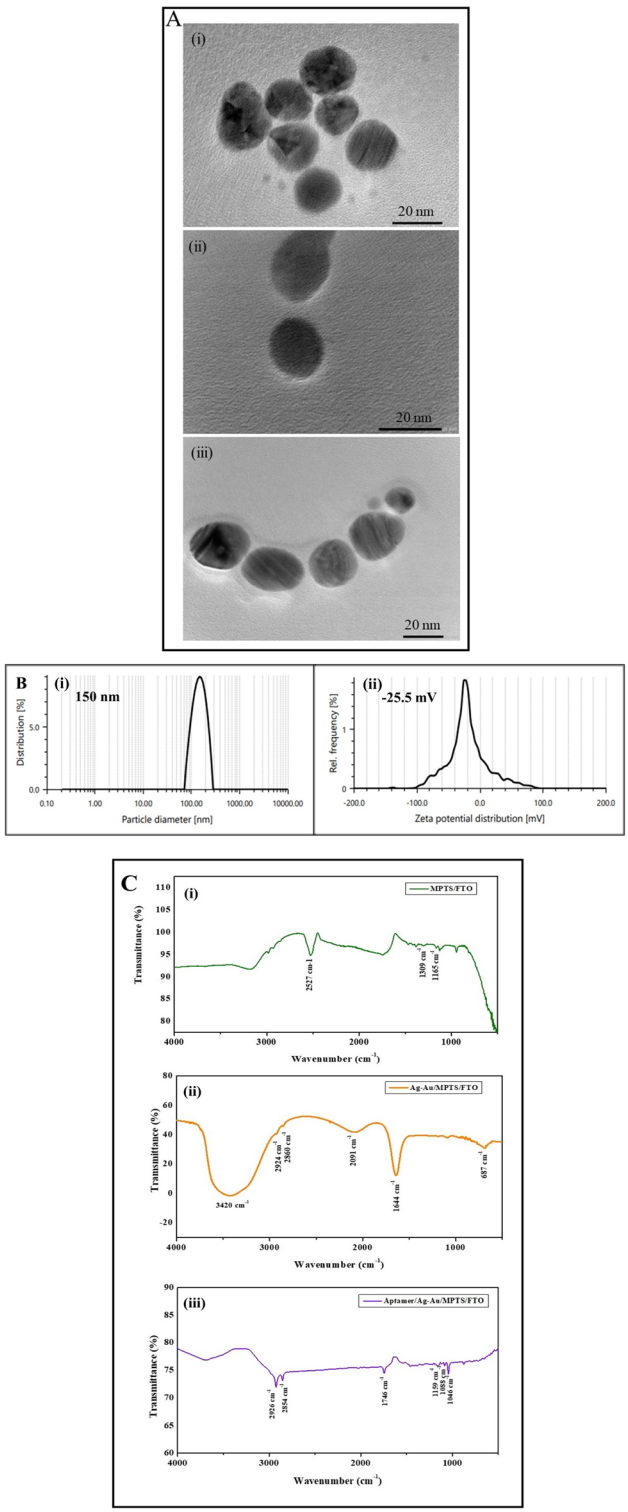

Fig. 2 (A) TEM images of (i) Ag NPs, (ii) Au NPs, (iii) Bimetallic Ag–Au NPs (B) DLS-ZETA analysis of green-synthesized bimetallic Ag–Au NPs (i) hydrodynamic diameter, (ii) zeta potential distribution, (C) FT-IR spectrum of (i) MPTS/FTO, (ii) Ag–Au/MPTS/FTO, (iii) aptamer/Ag–Au/MPTS/FTO electrode.

fringes, indicating the presence of well-defined crystal planes, enhanced crystallinity and surface reactivity.

The green synthesized Ag–Au NPs are subjected to Dynamic Light Scattering (DLS) technique to determine the average hydrodynamic particle size distribution and polydispersity index (PDI). The hydrodynamic diameter is the effective diameter of a nanoparticle in a solution, which consider both the particle and the surrounding layer of solvent molecules while

PDI measures the size distribution of nanoparticles in a sample. The study was carried by preparing a homogeneous solution of Ag–Au NPs by diluting 1 mg mL^{-1} NPs in Milli-Q water and ultrasonication for 30 minutes followed by subjecting to DLS analysis. Fig. 2B(i) reveals that the green synthesized Ag–Au NPs have a hydrodynamic diameter of 150.88 nm and a polydispersity index of 0.13, indicating fairly uniform size distribution of the particles in the solvent. As, DLS measures the hydrodynamic diameter of NPs, it often results in particle sizes larger than their actual size.[31] Furthermore, Fig. 2B(ii) indicates a mean zeta potential value of −25.5 mV signifying that the Ag–Au NPs possess a strong surface charge, which helps prevent their aggregation and promotes stability in the solution.[32] Hence, DLS-ZETA findings confirm synthesis of quite stable Ag–Au NPs with good dispersion, making them ideal for sensing platform.

Fig. 2C depicts the FTIR spectrum of (i) MPTS/FTO, (ii) Ag–Au/MPTS/FTO, and (iii) aptamer/Ag–Au/MPTS/FTO. MPTS/FTO electrode shows peak at 2527 cm^{-1} indicating the presence of thiol (–SH) group in MPTS molecule. The peaks at 1309 cm^{-1} and 1165 cm^{-1} corresponds to Si–O–Si confirming silane bonding to the FTO surface. The FTIR spectra of Ag–Au/MPTS/FTO indicates the disappearance of the –SH peak signifying successful binding of thiol groups to Ag–Au NPs. Also, appearance of peak around 687 cm^{-1} suggests metal–S interactions, confirming NPs attachment to MPTS surface. Further, broad peak at 3420 cm^{-1} indicates O–H stretching from phenolic compounds, while peaks at 2924 cm^{-1} and 2860 cm^{-1} demonstrates the presence of aliphatic chains from organic compounds. Furthermore, peak at 1644 cm^{-1} corresponds to C=O stretching indicating presence of phenolic-rich extract as stabilizing agent. The FTIR spectrum of the aptamer/Ag–Au/MPTS/FTO electrode reveals characteristic functional groups associated with aptamer immobilization. The transmittance peaks at 2926 cm^{-1} and 2854 cm^{-1} correspond to C–H and N–H stretching, respectively. A peak at 1746 cm^{-1}, typically associated with C=O stretching which may corresponds to the functional groups present in the aptamer structure, such as carbonyl groups in nucleotide bases. The peak at 1159 cm^{-1} corresponds to PO_4^{2-} stretching, confirming the presence of the phosphate backbone. Additionally, peaks at 1088 cm^{-1} and 1046 cm^{-1} are attributed to C–O stretching and asymmetric PO_2^- vibrations respectively that are indicative of nucleic acid structures. Notably, the absence of a strong S–H stretching peak 2550 cm^{-1} confirms the successful thiol-metal interaction, validating aptamer immobilization onto the electrode surface as demonstrated in Fig. 1C(iii).

3.2 Electrochemical characteristics of apta-electrode

DPV, CV and EIS techniques were employed to study the behaviour of the modified electrodes. DPV study was carried out in 50 mM PBS solution (pH = 7.0) containing 5 mM $[Fe(CN)_6]^{3-/4-}$ as a redox probe within a potential range of −0.2 V to 0.9 V. Fig. 3A shows a significant increase in DPV current (8.33×10^{-4} A) after the deposition of bimetallic Ag–Au NPs onto the MPTS/FTO electrode due to the conductive properties of green synthesised bimetallic Ag–Au NPs. In comparison, individual Ag and Au NPs, deposited as Ag/MPTS/FTO and Au/MPTS/FTO, exhibited lower DPV currents of 6.48×10^{-4} A and 5.60×10^{-4} A, respectively. Peak current of 3.81×10^{-4} A was seen in case of MPTS modified electrode. After the immobilization of aptamer onto the Ag–Au/MPTS/FTO fabricated electrode, peak current value decreased to (5.89×10^{-4} A) due to the insulating nature of the oligonucleotides which hinders the electron transfer. Furthermore, incorporation of MCH onto the aptamer modified electrode resulted in low current response (5.36×10^{-4} A). Subsequently, the current furthermore decreased (2.82×10^{-4} A) when the analyte (ampicillin) was introduced onto the modified MCH/Apt/Ag–Au/MPTS/FTO electrode surface showing formation of aptamer–ampicillin complex which further insulated the electrode surface and obstructed the diffusion of electroactive species to the working electrode.

Fig. 3B shows cyclic voltammogram of MPTS modified FTO, Ag/MPTS/FTO, Au/MPTS/FTO, Ag–Au/MPTS/FTO, aptamer/Ag–Au/MPTS/FTO, MCH modified apta-electrode, and an ampicillin treated apta-electrode with 10 μL of 1 μg mL^{-1} in 5 mM $Fe(CN)_6^{4-/3-}$ solution at a scan rate of 50 mV s^{-1} within a potential range of −0.6 to 1.2 V. The CV analysis reveals the current value of MPTS/FTO electrode to be 3.77×10^{-4} A (curve (i)). Further, (curve (iv)) demonstrates a significant increase in the current (1.07×10^{-3} A) after the deposition of bimetallic Ag–Au NPs onto the MPTS/FTO electrode, which could be attributed to the enhanced electron transfer efficiency due to their excellent electrical conductivity, nanoscale size and synergistic effect between Ag and Au NPs. In contrast, the monometallic Ag/MPTS/FTO (curve ii) and Au/MPTS/FTO (curve iii) electrodes showed lower currents of 8.01×10^{-4} A and 5.91×10^{-4} A, respectively, highlighting the advantage of the bimetallic configuration. Curve (v) shows a decrease in current (4.63×10^{-4} A) after modifying the Ag–Au/MPTS/FTO electrode with thiolated-aptamer, which can be due to the strong binding of the aptamer to the bimetallic NPs, forming a strong and compact layer on the electrode surface, thereby limiting electron transfer and reducing overall electrochemical activity. To enhance the stability of the aptamer and to avoid non-specific bindings, modification of the immobilization support with MCH, a blocking agent, leads to further decrease in current (4.60×10^{-4} A) (curve (vi)). Curve (vii) shows further decrease in current (2.05×10^{-4} A) after incubation with ampicillin due to the formation of aptamer–ampicillin complex confirming successful fabrication of the apta-electrode. The CV results of all the modified electrodes (MPTS/FTO; Ag/MPTS/FTO; Au/MPTS/FTO; Ag–Au/MPTS/FTO; aptamer/Ag–Au/MPTS/FTO; MCH/Apt/Ag–Au/MPTS/FTO; ampicillin/MCH/Apt/Ag–Au/MPTS/FTO) well align with the DPV studies.

Along with DPV and CV, EIS technique was also employed to study the features of electrode–electrolyte interface Fig. 3C. EIS studies were conducted within the frequency range of 0.1–10^5 Hz operating at the open circuit potential of + 0.25 V with the excitation amplitude of 10 mV. The obtained Nyquist plots were also interpreted using NOVA software and the data was fitted into an equivalent circuit [R[Q(RW)]]. The individually

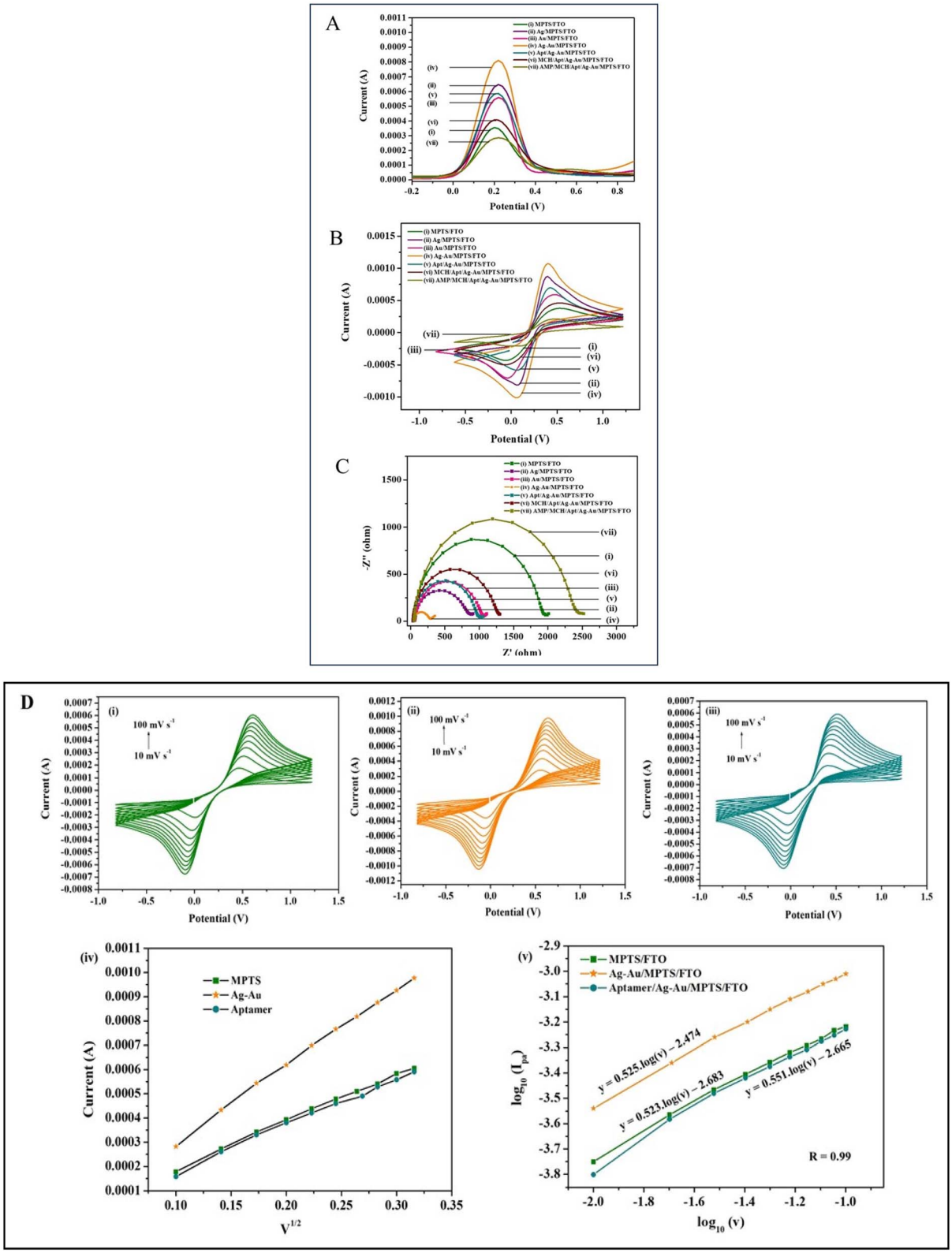

Fig. 3 (A) DPV response of (i) MPTS/FTO, (ii) Ag/MPTS/FTO, (iii) Au/MPTS/FTO (iv) Ag–Au/MPTS/FTO, (v) aptamer/Ag–Au/MPTS/FTO, (vi) MCH/aptamer/Ag–Au/MPTS/FTO and (vii) ampicillin/MCH/aptamer/Ag–Au/MPTS/FTO, (B) CV response of (i) MPTS/FTO, (ii) Ag/MPTS/FTO, (iii) Au/MPTS/FTO (iv) Ag–Au/MPTS/FTO, (v) aptamer/Ag–Au/MPTS/FTO, (vi) MCH/aptamer/Ag–Au/MPTS/FTO and (vii) ampicillin/MCH/aptamer/Ag–Au/MPTS/FTO. (C) Nyquist plots of (i) MPTS/FTO, (ii) Ag/MPTS/FTO, (iii) Au/MPTS/FTO (iv) Ag–Au/MPTS/FTO, (v) aptamer/Ag–Au/MPTS/FTO, (vi) MCH/aptamer/Ag–Au/MPTS/FTO and (vii) ampicillin/MCH/aptamer/Ag–Au/MPTS/FTO, (D) CV response of (i) MPTS/FTO, (ii) Ag–Au/MPTS/FTO, (iii) aptamer/Ag–Au/MPTS/FTO at different scan rate within 10–100 mV s^{-1} in $[Fe(CN)_6]^{3-/4-}$ electrolyte, (iv) Plot between I_{pa} and $\nu^{1/2}$ for different modified FTOs and (v) Plot of $\log_{10}(I_{pa})$ and $\log_{10}(\nu)$ for different modified electrodes.

modified monometallic electrodes – Ag/MPTS/FTO (plot ii) and Au/MPTS/FTO (plot iii) exhibited higher R_{ct} values of 792.7 Ω and 971.5 Ω, respectively, reflecting their comparatively lower conductivity. This clearly highlights the enhanced charge transfer ability of the bimetallic Ag–Au/MPTS/FTO electrode (plot iv), which benefits from the synergistic effect between Ag and Au nanoparticles, resulting in a significantly reduced R_{ct} of 193.19 Ω. Further, the R_{ct} value of MPTS modified FTO was (1862.6 Ω) as displayed in (plot (i)). It has been observed that upon modifications with aptamer the R_{ct} value (933.83 Ω) increased (plot (v)) indicating that the modification with aptamer resists the flow of electrons due to its bulky nature ensuring the formation of thick layer of aptamer after binding with the Ag–Au NPs covering the electrode surface. Furthermore, gradual increase in R_{ct} values (1202.5 Ω) and (2406.9 Ω) after modifying with MCH and ampicillin was seen as shown in (plot (vi) and (vii)) respectively that is attributed to the non-conducting nature of the molecules. The addition of ampicillin forms compact insulating layer onto the electrode surface reducing electron transfer efficiency. The formation of aptamer–ampicillin complex induces a conformational change, hindering electron flow at the electrode surface. Hence, the EIS analysis well corresponds with the CV and DPV analysis, confirming the successful fabrication of the matrix.

3.2.1 Evaluation of electroactive surface area and electrode kinetics. While evaluating the response of the electrochemical system, a crucial parameter to consider is the electroactive surface area of the working electrode, as the peak current (I_{pa}) depends on it. CV study was employed to study the electrochemical mechanism and electrode kinetics in the presence of a redox species $[Fe(CN)_6]^{3-/4-}$ as an electrolyte at various scan rates (ν) ranging from 10 to 100 mV s^{-1}. The corresponding cyclic voltammograms exhibited a gradual increase in peak current with increasing scan rates as depicted in Fig. 3D(i–iii). This linear variation in current was observed consistently across each modification step indicating a stable, quasi-reversible redox behaviour and a diffusion-mediated process. Fig. 3D(v) shows logarithmic plot of maximum current *versus* scan rate and the slope value near 0.5 indicates that the redox process follows a diffusion-mediated mechanism.[33] The peak current data were plotted against square root of the scan rate as demonstrated in Fig. 3D(iv), and the resulting linear fit (R = 0.99) demonstrated good correlation. The slope and intercept values obtained from the regression analysis were subsequently incorporated into the Randles–Sevcik equation.

$$I_{pa} = 2.69 \times 10^5 A_e n^{3/2} C D^{1/2} \nu^{1/2} \quad (1)$$

where, I_{pa} is the anodic peak current (A), A is the electrode area (cm^2), n is the number of electrons transferred, C_o is the concentration of the redox-active species in the electrolyte (5 mmol cm^{-3} $[Fe(CN)_6]^{3-/4-}$), D is the diffusion coefficient (7.6×10^{-6} cm^2 s^{-1}), ν is the scan rate (V s^{-1}).

$$I_{pa\ (MPTS/FTO)} = 19.6 \times 10^{-4}\ A\ (V\ s^{-1})^{-1/2}\ \nu^{1/2} - 4.87\ \mu A \quad (2)$$

$$I_{pa\ (Ag–Au/MPTS/FTO)} = 31.7 \times 10^{-4}\ A\ (V\ s^{-1})^{-1/2}\ \nu^{1/2} - 1.67\ \mu A \quad (3)$$

$$I_{pa\ (aptamer/Ag–Au/MPTS/FTO)} = 19.3 \times 10^{-4}\ A\ (V\ s^{-1})^{-1/2}\ \nu^{1/2} - 1.57\ \mu A \quad (4)$$

The electroactive surface area obtained for each modified electrode was as follows: 0.527 cm^2 for MPTS/FTO, 0.857 cm^2 for Ag–Au/MPTS/FTO electrode, and 0.521 cm^2 for aptamer/Ag–Au/MPTS/FTO electrode indicating the highest electroactive surface area for the electrode modified with green-synthesized NPs, attributed to their enhanced surface characteristics and effective interaction with redox species making them suitable for sensing platform. Further, the surface concentration of redox species (I^*) at a specific time on each modified electrode was determined using the Brown–Anson model.[34]

$$I_{pa} = n^2 F^2 I^* \times A\nu / 4RT \quad (5)$$

where, I_{pa} represents the anodic peak current (A), n is the number of electrons involved in the redox process ($n = 1$), F is the Faraday constant (96 485.33 C mol^{-1}), A is the electrode's geometrical surface area (0.36 cm^2), ν is the scan rate used during CV (50 mV s^{-1}), R is the gas constant (8.314 J K^{-1} mol^{-1}), and T is the temperature (298.15 K). The I^* value for each modified electrode is given in Table 1. The green-synthesized Ag–Au NPs modified electrode exhibited the highest (I^*) value, indicating the highest surface concentration of redox species on the modified electrode.

Additionally, the electrochemical behaviour was evaluated through impedance measurements at the electrode–electrolyte interface. The charge transfer resistance (R_{ct}) values for each modified electrode are listed in Table 1, with the green-synthesized nanoparticles exhibiting the lowest impedance, confirming enhanced charge transfer efficiency.

The R_{ct} values obtained from the fitting analysis was then utilized to evaluate the electron transfer kinetics at each electrode, specifically focusing on the exchange current density (i_o) and the apparent electron transfer rate constant (K_{app}). These parameters were calculated using the following equations:

$$i_o = nRT / R_{ct} F \quad (6)$$

$$K_{app} = RT / n^2 F^2 A R_{ct} C \quad (7)$$

All the variables used in the calculations have been defined and explained earlier. After incorporating all the variables in eqn (6) and (7) the values obtained were mentioned in Table 1. In conclusion, both the electrode kinetics and electrochemical assessment highlighted the enhanced electro-catalytic performance of the green-synthesized Ag–Au NPs making them a suitable choice as effective sensing platform strategy.

3.3 Optimization study

To achieve high-performance electroanalytical detection of ampicillin, optimization of biorecognition element concentration, immobilization time, and response time was carried out using DPV technique. The SH-modified aptamer was immobilized onto the Ag–Au/MPTS/FTO electrode with varying concentrations such as 1 μM, 5 μM, 10 μM, 15 μM, 20 μM and 25 μM. It was observed

Table 1 Electrochemical parameters of modified electrodes

Working electrode	I_{pa} (A)	I^* (mol cm^{-2})	A_e (cm^2)	R_{ct} (Ω)	i_o (A cm^{-2})	K_{app} (cm s^{-1})
MPTS/FTO	3.77×10^{-4}	1.12×10^{-9}	0.527	1862.6	13.79	0.44×10^{-6}
Ag–Au/MPTS/FTO	1.03×10^{-3}	3.04×10^{-9}	0.857	193.19	132.98	7.66×10^{-4}
Aptamer/Ag–Au/MPTS/FTO	4.63×10^{-4}	1.37×10^{-9}	0.521	933.83	27.51	1.58×10^{-4}

that the peak current value decreased as the aptamer concentration increases, up to 10 μM. Beyond this concentration, no further decrease in current was seen making 10 μM the optimal concentration for detecting ampicillin (Fig. 4A). Further, 10 μM aptamer concentration was applied on different electrodes for varying time intervals, such as 5, 30, 60, 90, 120, and 150 min. The change in peak current with respect to incubation time was also monitored. It was observed that after 90 min of incubation, there was no significant decrease in peak current, suggesting that 90 min is sufficient for optimal aptamer binding to the Ag–Au/MPTS/FTO electrode (Fig. 4B). Further to this, the time required for the formation of the aptamer–antibiotic complex was examined. It was found that as the binding time increases, the current response gradually decreases which was stabilized after 15 min. Therefore, 15 min was selected as the optimal binding time for additional experiments (Fig. 4C).

3.4 Analytical performance and interference study

The efficiency of the fabricated MCH/aptamer/Ag–Au/MPTS/FTO electrode sensor was assessed across different concentrations of ampicillin using DPV technique under the optimised conditions. Fig. 5A shows the current response of ampicillin/MCH/aptamer/Ag–Au/MPTS/FTO electrode when incubated with different concentrations of ampicillin from 0.1 ng mL^{-1} to 1000 ng mL^{-1}. The result showed gradual decrease in the peak current value with increased concentration of ampicillin as represented in the Fig. 5B. The decrease might be because, as ampicillin concentration increases, the aptamer–antibiotic complex becomes more stable, causing steric hindrance that limits the diffusion of electro-active species to the working electrode and reduces the current response. A calibration plot is also given in the (Fig. 5C) between the log of ampicillin concentrations v/s current responses. The slope value obtained from the calibration plot was used to calculate various performance metrics such as the theoretical LOD (3 × standard deviation (SD)/m), LOQ (10 × SD/m) and sensitivity (m/electro active surface area (a)) where 'm' is the slope of calibration plot. The proposed sensor exhibited linearity within the concentration range of 0.1 ng mL^{-1} to 1000 ng mL^{-1} following the linear fit equation as:

$$Y = -6.01 \times 10^{-5} X + 4.66 \times 10^{-4} \quad (8)$$

Additionally, the calculated values of the LOD, LOQ and sensitivity were found to be 0.4 ng mL^{-1}, 1.36 ng mL^{-1}, and 9.93 μA (ng mL^{-1})$^{-1}$ cm^{-2}, respectively.

In order to further investigate the performance of the sensor, its ability to distinguish between the target antibiotic and non-target antibiotics, in a complex medium like milk, is another important parameter. In Fig. 5D, a comparative study was conducted by measuring the current response of the antibiotic–

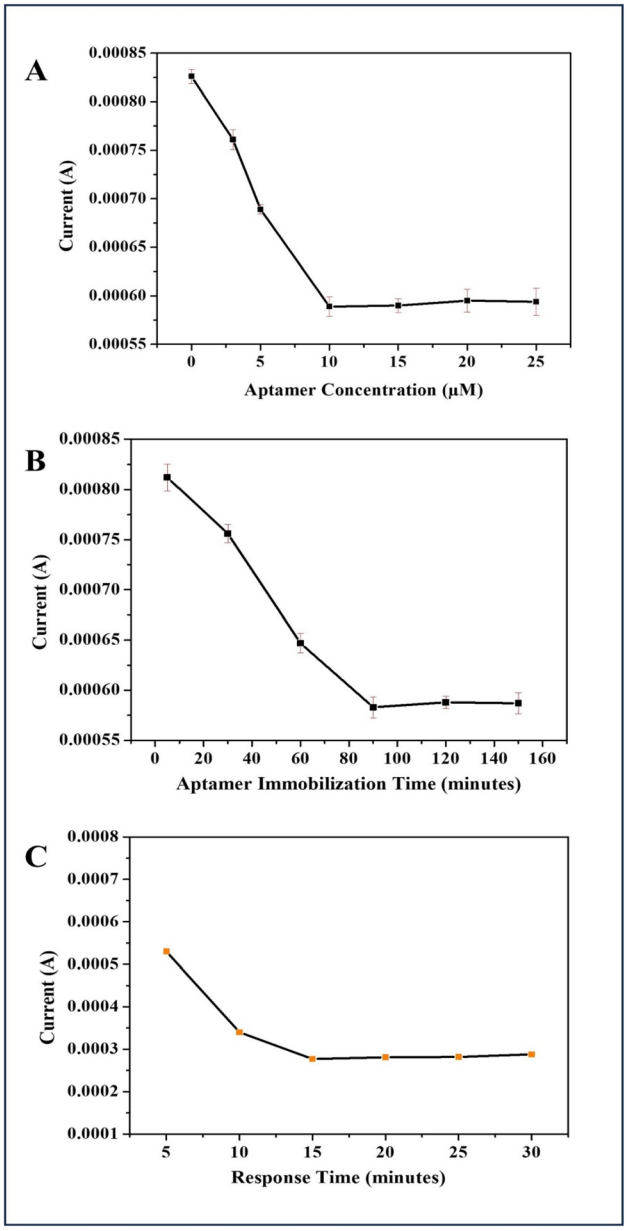

Fig. 4 (A) The DPV response of aptamer/Ag–Au/MPTS/FTO against incubation with different concentrations of thiolated-aptamer, (B) the variation of I_p value with different immobilization time of aptamer onto Ag–Au/MPTS/FTO electrode and (C) variation of I_p value of MCH/aptamer/Ag–Au/MPTS/FTO incubated with ampicillin for varying time intervals, all recorded using $[Fe(CN)_6]^{3-/4-}$ redox mediator as electrolyte.

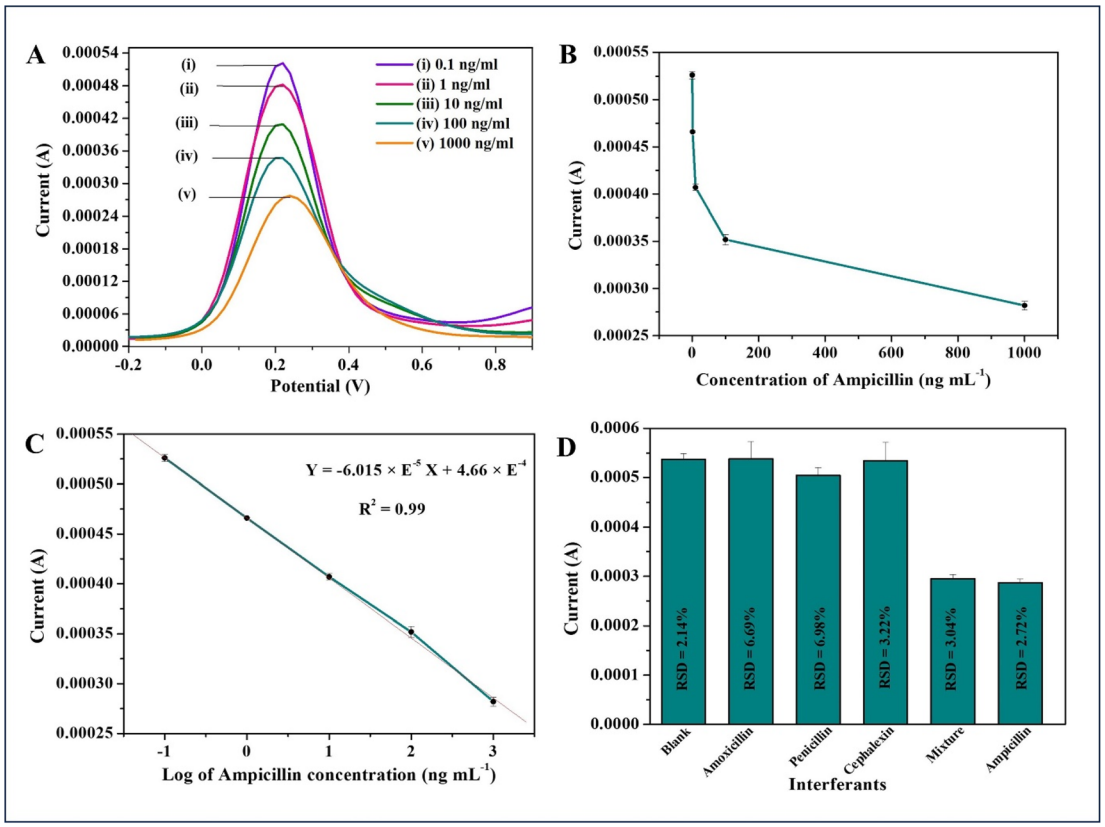

Fig. 5 (A) I_p plot at varying concentrations of ampicillin (0.1 to 1000 ng mL^{-1}), (B) variation of DPV current response with different concentrations of ampicillin ranging from 0.1 to 1000 ng mL^{-1}, (C) the calibration plot depicts the variation of peak current with log of ampicillin concentrations which exhibited a linear response, (D) Bar graph showing DPV current values of aptasensor for detection of different beta-lactam antibiotics and their mixture compared with blank.

aptamer complex on the apta-electrodes, which were employed with the target antibiotic (ampicillin), non-target antibiotics (such as amoxicillin, cephalexin and penicillin) and a mixture of all antibiotics used in this study. Since ampicillin is a beta-lactam antibiotic, other beta-lactam antibiotics were selected for the interference study to assess the sensor's ability to specifically detect ampicillin in the presence of structurally similar compounds, thereby ensuring its specificity within the same class of antibiotics. The DPV current response significantly decreased in case of ampicillin and the mixture solution of all antibiotics including ampicillin while non-target antibiotic electrodes exhibited a slight change nearly identical to that of blank electrode. This likely resulted from the specific binding of ampicillin to the aptamer, demonstrating the efficacy of the aptasensor to selectively detect ampicillin.

Further to assess the applicability of the developed sensor in real samples, spike-in study as well as real sample testing was also performed to estimate ampicillin concentration and the results obtained were then compared with LC-MS technique for validation mentioned in the Section 3.7.

3.5 Reproducibility and shelf-life of the sensor

Reproducibility of the proposed sensor was evaluated through intra-assay and inter-assay studies. As seen in Fig. 6A–C a total of 42 MCH/aptamer/Ag–Au/MPTS/FTO electrodes were prepared which were then divided into six sets of seven electrodes. For intra-assay study (same day) three sets were incubated with ampicillin at three different concentrations of 0.1 ng mL^{-1}, 1 ng mL^{-1}, and 1000 ng mL^{-1}, respectively. Similarly, for inter-assay study (for seven consecutive days) other three sets were incubated with ampicillin with aforementioned concentrations. Results were assessed in terms of relative standard deviation value (RSD value). The RSD for intra-assay study was 1.53%, 1.81%, and 2.90% at concentrations of 0.1 ng mL^{-1}, 10 ng mL^{-1}, and 1 μg mL^{-1}, respectively, while for inter-assay study, the RSD values were 1.79%, 1.88%, and 3.29% at the same concentrations. Overall, the RSD ranged from 1.53% to 3.29%, indicating high reproducibility and accuracy of the sensor.

Further, to evaluate the shelf-life of the proposed aptasensor, stability study was performed by storing the apta-electrodes at 4 °C for 35 days followed by electrochemical determination of ampicillin at an interval of 5 days. As depicted from Fig. 6D the DPV current response exhibited a slight decline of 5.4% on 30th day and maintained 87.6% of its output until 35th day indicating a shelf-life of 30 days.

3.6 Spike-in study

To assess the credibility of the proposed aptasensor, different concentrations of ampicillin were spiked into milk sample (initially having no detectable ampicillin prior to spike-in study)

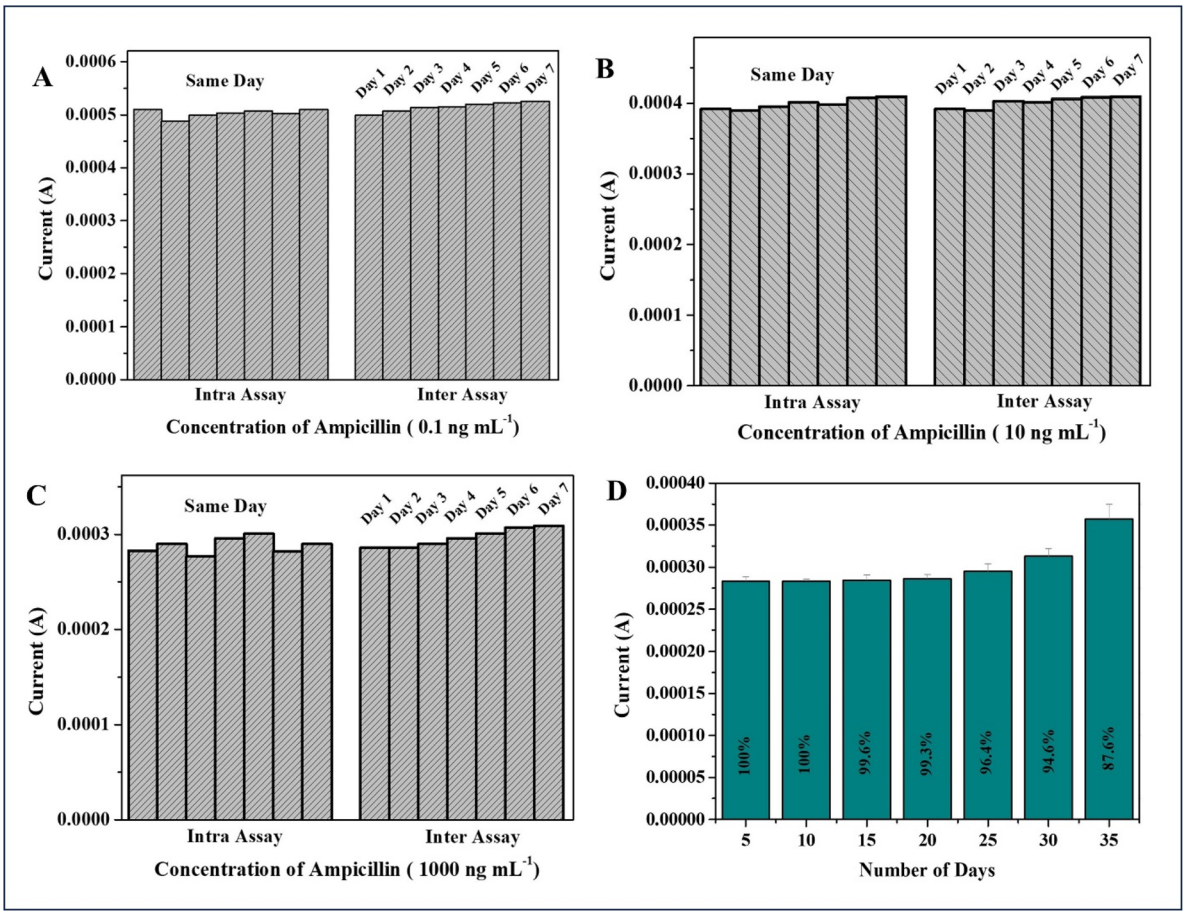

Fig. 6 The peak current value of MCH/aptamer/Ag–Au/MPTS/FTO towards intra assay (same day) and inter assay (for consecutive days) detection of (A) 0.1 ng mL^{-1}, (B) 10 ng mL^{-1} and (C) 1 μg mL^{-1}, ampicillin concentrations, (D) the variation of peak current value of MCH/aptamer/Ag–Au/MPTS/FTO electrode towards detection of ampicillin at an interval of 5 days for a total duration of 35 days.

and corresponding DPV analysis was carried out. The peak current (I_p) values obtained from the spiked sample were correlated with the standard calibration curve to calculate the found concentration and recovery percentage, as summarized in Table 2, using the given formula:

$$\text{Found conc.} = \text{spiked } I_p/\text{standard } I_p \times \text{conc. spiked} \quad (9)$$

$$\text{Recovery \%} = \text{conc. found/conc. spiked} \times 100 \quad (10)$$

Fig. 7A displays significant alignment of spike-in analysis with the standard calibration plot, confirming reliable performance of the aptasensor in spiked milk sample, with a recovery percentage ranging from 94.1% to 104.2% and an RSD value between 2.02% and 3.78% as mentioned in Table 2.

3.7 Real-world milk testing for ampicillin and validation using LC-MS technique

The practical applicability of the developed aptasensor was assessed to evaluate its performance. Fig. 7B and C demonstrates the analysis of milk samples collected from four different local vendors (T1, T2, T3, and T4), using both the present aptasensor and LC-MS technique. The procedure for preparing sample is utilized from the literature.[35] Briefly, 4 mL milk sample was taken and mixed with 20 mL of 75% acetonitrile solution and vortexed for 10 min. The mixture was then centrifuged at 8000 rpm for 12 minutes to precipitate milk proteins. Subsequently, the supernatant was filtered through 0.22 μm membrane to eliminate lipids. Following this, the prepared samples were analysed using the developed aptasensor and LC-MS technique for validation.

As shown in Table 3, LC-MS technique detected ampicillin at a concentration of 200 ng mL^{-1} in sample T1, whereas no ampicillin was detected in sample T2, T3, and T4. Likewise, the

Table 2 Recovery % obtained from spike-in study

S. no.	Concentration spiked (ng mL^{-1})	Concentration found (ng mL^{-1})	Recovery (%)	RSD (%)
1	0.1	0.101	101	3.17
2	1	1.023	102	2.62
3	10	9.410	94.1	2.02
4	100	99.43	99.4	2.71
5	1000	1042.5	104.2	3.78

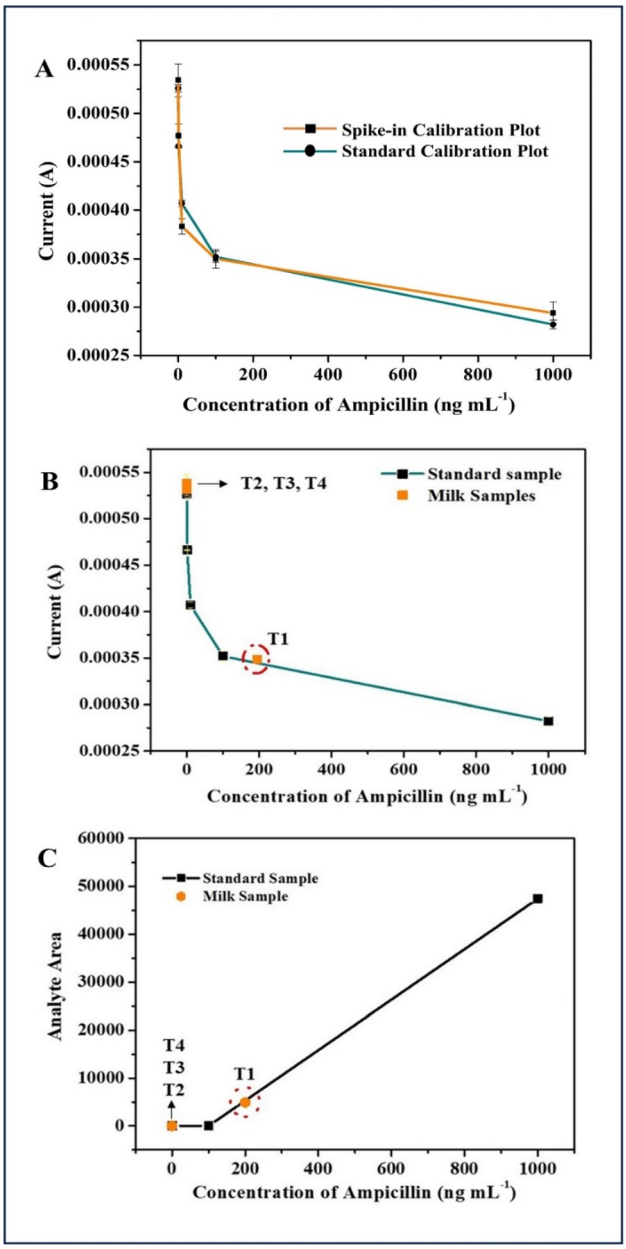

Fig. 7 (A) Calibration plot of peak current (I_p) *vs.* different concentrations of ampicillin within a linear range (0.1 ng mL^{-1}–1000 ng mL^{-1}) along with its comparison with standard calibration plot (B) electrochemical response of the present aptasensor to ampicillin detection in 4 different unknown milk samples (T1, T2, T3 and T4), (C) LC-MS response to ampicillin detection in same 4 different unknown milk samples (T1, T2, T3 and T4).

Table 3 Comparison of present aptasensor with LC-MS technique in real milk samples

S. no.	Sample ID	DPV technique (ng mL^{-1})	LC-MS technique (ng mL^{-1})
1	T1	194	200
2	T2	Non-detectable	Non-detectable
3	T3	Non-detectable	Non-detectable
4	T4	Non-detectable	Non-detectable

present aptasensor quantified ampicillin at a concentration of 194 ng mL^{-1} in T1, with no detectable levels observed in the other samples. The strong correlation between both methods confirms the accuracy of the proposed aptasensor. Additionally, validation with LC-MS technique further supports the effectiveness of the developed aptasensor for ampicillin detection in real samples.

4 Conclusion

The Ag–Au NPs were initially synthesised using a green approach and subsequently employed for the fabrication of an electrochemical biosensor for the detection of ampicillin residues in milk. The NPs were deposited onto the electrode surface through MPTS functionalization and employed to bind aptamers through thiol-based chemistry. Furthermore, limit of detection, sensitivity, reproducibility and stability were also determined. The developed aptasensor exhibited appreciable LOD of about 0.40 ng mL^{-1} with a response time of 15 min. The sensor also showed a shelf life of about 30 days at 4 °C. The developed sensor has been tested with the real samples and the results are in sync with LC-MS studies. Hence, the green synthesized Ag–Au NPs based sensor demonstrated remarkable properties, such as excellent surface functionality, stability and highly sensitive and selective detection of ampicillin. The proposed sensor can be utilised for detection of ampicillin residues in various mediums beyond milk, ensuring broader applicability. Also, the presence of other antibiotics can be explored by developing microarray-based sensor for multiplex detection using green synthesized Ag–Au NPs as sensing platform.

Data availability

All the data associated with this research have been presented in this paper.

Conflicts of interest

There are no conflicts to declare.

Acknowledgements

This work is supported by UGC grants (Reference Number: 221610015920) and (Reference Number: 201610127295). The authors are truly thankful to the Sophisticated Analytical Instrumentation Facility/Central Instrumentation Laboratory (SAIF/CIL), Panjab University, Chandigarh, for their support in the characterization studies.

References

1 P. Singhal, in *Safety Issues in Beverage Production*, ed. A. M. Grumezescu and A. M. Holban, Academic Press, 2020, ch. 12, pp. 399–427.
2 M. Virto, G. Santamarina-García, G. Amores and I. Hernández, *Dairy*, 2022, **3**, 541–564.

3 R. Omairi, M. Krayem, S. Khaled, M. Salla and S. El Khatib, *World J. Pharmacol.*, 2022, **11**, 48–55.
4 D. Kaushik, M. Mohan, D. M. Borade and O. C. Swami, *J. Clin. Diagn. Res.*, 2014, **8**, ME01–ME03.
5 E. Fernández-Varón, E. Escudero-Pastor and C. M. Cárceles-Rodríguez, *Vet. J.*, 2005, **169**, 437–443.
6 M. M. J. Arsène, A. K. L. Davares and P. I. Viktorovna, *Vet. World*, 2022, **15**, 662–671.
7 S. Sachi, J. Ferdous, M. H. Sikder and S. M. A. K. Hussani, *J. Adv. Vet. Anim. Res.*, 2019, **6**, 315–332.
8 M. Li, R. Li and Z. Li, *Microchim. Acta*, 2025, **192**, 15.
9 D. Nalbant, J. A. Reeder, P. Li, C. T. O'Sullivan, W. K. Rogers and G. An, *J. Pharm. Biomed. Anal.*, 2021, **196**, 113899.
10 H. Lin, F. Fang, J. Zang, J. Su, Q. Tian, R. Kumar Kankala and X. Lin, *Micromachines*, 2020, **11**, 431.
11 S. Rani, J. Kaur, A. Kaur, R. Rohilla, S. Devi, R. Sandhir and N. Prabhakar, *J. Mol. Struct.*, 2024, **1318**, 139174.
12 R. Rohilla, A. Kaur, S. Rani and N. Prabhakar, *Biosens. Bioelectron.*, 2025, **267**, 116783.
13 A. Kaur, S. Kapoor, A. Bharti, S. Rana, G. R. Chaudhary and N. Prabhakar, *J. Electroanal. Chem.*, 2020, **873**, 114400.
14 S. F. Ahmed, M. Mofijur, N. Rafa, A. T. Chowdhury, S. Chowdhury, M. Nahrin, A. B. M. S. Islam and H. C. Ong, *Environ. Res.*, 2022, **204**, 111967.
15 A. I. Osman, Y. Zhang, M. Farghali, *et al.*, *Environ. Chem. Lett.*, 2024, **22**, 841–887.
16 Food Safety and Standards Authority of India (FSSAI), **https://fssai.gov.in/upload/uploadfiles/files/Compendium_Contaminants_Regulations_28_01_2022.pdf**, accessed March 2025.
17 R. A. Banjara, A. Kumar, R. K. Aneshwari, M. L. Satnami and S. K. Sinha, *Environ. Nanotechnol. Monit. Manag.*, 2024, **22**, 100988.
18 M. Huston, M. DeBella, M. DiBella and A. Gupta, *Nanomaterials*, 2021, **11**, 2130.
19 K. Deka, R. D. Nongbet, K. Das, P. Saikia, S. Kaur, A. Talukder and B. Thakuria, *Hybrid Adv.*, 2025, **9**, 100399.
20 M. Ghasemi, M. Govahi and H. R. Litkohi, *Int. J. Biol. Macromol.*, 2025, **291**, 138619.
21 W. A. El-Said, A. Akhdhar, A. S. Al-Bogami and T. S. Saleh, *Spectrochim. Acta, Part A*, 2025, **327**, 125402.
22 R. V. Poonguzhali, E. R. Kumar, C. Srinivas, M. Alshareef, M. M. Aljohani, A. A. Keshk, N. M. El-Metwaly and N. Arunadevi, *Sens. Actuators, B*, 2023, **377**, 133036.
23 K. Sahu, R. Kurrey and A. Pillai, *RSC Adv.*, 2024, **14**, 23240–23256.
24 M. Kaur, A. Gautam, P. Guleria, K. Singh, V. Kumar and C. Opin, *Environ. Sci. Health.*, 2022, **29**, 100390.
25 H. Padalia, P. Moteriya and S. Chanda, *Arab. J. Chem.*, 2015, **8**, 732–741.
26 K. M. Song, E. Jeong, W. Jeon, M. Cho and C. Ban, *Anal. Bioanal. Chem.*, 2012, **402**, 2153–2161.
27 J. Santos, S. Toma, R. Yatsuzuka and K. Araki, *J. Braz. Chem. Soc.*, 2020, **31**, 2274–2281.
28 A. Kaur, R. Kumar, G. Chaudhary and N. Prabhakar, *J. Appl. Electrochem.*, 2023, **54**, 1–17.
29 H. S. Toh, C. Batchelor-McAuley, K. Tschulik, *et al.*, *Sci. China:Chem.*, 2014, **57**, 1199–1210.
30 M. Khan, K. Al-hamoud, Z. Liaqat, M. R. Shaik, F. Syed, M. Kuniyil, H. Alkhathlan, A. Al-Warthan, M. R. Siddiqui, M. Mondeshki, W. Tremel, M. Khan and M. Tahir, *Nanomaterials*, 2020, **10**, 91885, DOI: **10.3390/nano10091885**.
31 K. Khandare, S. Kumar, S. C. Sharma and S. Goswami, *Biochem. Biophys. Res. Commun.*, 2024, **739**, 150967.
32 S. Sikdar and M. Sikdar, *Bioresour. Technol. Rep.*, 2023, **24**, 101669.
33 S. Devi, S. Riedel, S. Döring, L. Hiller, A. K. S. Kumar, S. Flemig, C. Singh, Z. Konthur, V.-D. Hodoroaba and R. J. Schneider, *Sens. Actuators, B*, 2025, **431**, 137381.
34 H. Dhyani, M. A. Ali, S. Pal, S. Srivastava, P. Solanki, B. Malhotra and P. Sen, *RSC Adv.*, 2015, **5**, 45928–45934.
35 F. Tasci, H. S. Canbay and M. Doganturk, *Food Control*, 2021, **127**, 108147.